Investigation of a Novel Snout-Mounted Quad-Compton Camera system for In Vivo Proton Dose Verification via Prompt Gamma Imaging

Vijay R. Sharma, E. Shakeri, Z. Jiang, S. Mossahebi, A. Chalise, M. K. Gobbert, S. W. Peterson, J. C. Polf, and L. Ren

***Abstract*—This study presents a novel simulation study for integrating four Compton Cameras (CC) into proton therapy systems by mounting them directly on the snout of the treatment gantry for prompt gamma imaging (PGI). This compact, fixed geometry simplifies detector integration, maintains alignment with the proton beam axis, and supports in vivo proton range verification. A Geant4-based Monte Carlo framework, PJ-MC, was used to simulate prompt gamma emissions (PGE) in water and patient-specific geometry. PG image reconstruction was performed using the Kernel Weighted Back Projection (KWBP) algorithm. To improve range accuracy, we introduced a post-processing method called Point Source Normalization (PSN), which uses precomputed PGI responses for monoenergetic gamma point sources at different depths to normalize PGI images and correct distortions from attenuation, geometric factors, and detector responses from PGE detected curve. Simulations with monoenergetic sources confirmed the influence of depth-dependent attenuation and inverse square losses, especially at higher proton energies. Clinical beam energies of 70, 150, and 200 MeV were tested. KWBP reconstructions showed increasing range discrepancies with energy, reaching 176 mm (water) and 144 mm (patient) at 200 MeV. PSN correction reduced these errors by up to 70%, bringing PG hotspots closer to the Bragg peak (D_{max}). Simulations with anterior/posterior shifts showed that the PSN-corrected system could detect millimeter-scale range deviations from setup uncertainties and beam shifts. This is the first study to simulate and evaluate a snout-mounted CC system for PGI in proton therapy. Results support future validation under clinical beam conditions in phantoms and patients.**

***Index Terms*—IEEE, IEEEtran, journal, LaTeX, paper, template.**

I. Introduction

PROTON therapy is a type of radiation therapy that uses protons to treat cancer. Its main advantage lies in the physical property of protons to deposit most of their energy at a specific depth in tissue, known as the Bragg peak. This allows for highly localized dose delivery to the tumor while sparing surrounding healthy tissues. However, a key challenge in clinical practice is the uncertainty in predicting the exact proton range inside the patient's body. These uncertainties can arise from patient setup errors, anatomical changes, or limitations in converting computed tomography (CT) Hounsfield units (HU) into relative proton stopping power. Even small range errors can lead to under-dosing the tumor or damaging healthy tissues.

To address this issue, researchers have explored various methods for in vivo verification of the proton beam range. One promising approach involves detecting secondary gamma rays produced when protons interact with tissue [1], [2], [3], [4], [5]. These interactions generate two main types of gamma emissions: positron annihilation (PA) gammas and prompt gammas (PGs). PA gammas result from radioactive isotopes created by the beam, emitting positrons that annihilate with electrons to produce 511 keV photons. In contrast, PGs are emitted almost instantaneously as excited nuclei return to their ground state. Different nuclei emit PGs at characteristic energies and analyzing the PG spectrum can reveal the spatial distribution of proton interactions.

Recent research has shown a strong correlation between the spatial distribution of PG emissions and the location of proton dose deposition (D_{max}). This relationship has been demonstrated through both experimental measurements and Monte Carlo (MC) simulations in simple phantoms [6], [7], [8] as well as in more realistic, patient-specific geometries derived from CT imaging [9], [10], [11]. These findings support PGI as a viable method for in vivo range verification to reduce dose uncertainties in proton therapy.

Although PGs provide valuable information for proton range verification, they have much higher energies (typically between 2 and 10 MeV) than gamma rays used in PET or SPECT ($<$1 MeV), making standard medical gamma detectors unsuitable for PGI [12], [13], [14]. This limitation has driven the development of dedicated imaging systems for prompt gamma detection in clinical settings [15], [16], [17], [18]. Among them, the slit-camera system has been widely studied, using a tungsten collimator to accept PGs from a narrow field including the recent study by Berthold et al. [19], which investigated its ability to monitor anatomical changes during prostate cancer treatment. Clinical trials, including a first-in-human study, demonstrated its use for monitoring anatomical

V. R. Sharma is with the Department of Radiation Oncology, School of Medicine, University of Maryland, Baltimore, MD, USA, and with the Department of Medical Physics, University of Wisconsin–Madison, Madison, WI, USA (e-mail: vsharma@wisc.edu).

E. Shakeri and M. K. Gobbert are with the Department of Mathematics and Statistics, University of Maryland Baltimore County, Baltimore, MD, USA.

Z. Jiang is with the Department of Radiation Oncology, Stanford University, Stanford, CA 94304, USA.

S. Mossahebi, A. Chalise, and L. Ren are with the Department of Radiation Oncology, School of Medicine, University of Maryland, Baltimore, MD, USA (corresponding author: L. Ren, e-mail: lren@som.umaryland.edu).

S. W. Peterson is with the Department of Physics, University of Cape Town, Rondebosch 7700, South Africa.

J. C. Polf is with M3D, Ann Arbor, MI 48108, USA (e-mail: jpolf@m3dimaging.com).

This work did not involve any human participants or animal studies.

changes during prostate treatment [19]. Its high detection efficiency is beneficial for low-signal conditions in spot-scanning proton therapy. However, slit cameras provide only 1D profiles and do not support 2D or 3D reconstruction. Their distal falloff is not sharply defined and is influenced by beam position, patient anatomy, and detector placement. Range verification depends on comparing measured PG distributions to reference simulations, making accuracy sensitive to geometric and tissue uncertainties. Another key limitation is detector placement. Most setups locate detectors beneath the treatment couch or adjacent to the patient, which poses challenges for clinical integration due to spatial constraints, hardware complexity, and cable routing. Varying beam angles further change the relative orientation between the detector and beam, introducing image distortions that are hard to correct.

As such, PGI has advanced in both hardware and software. Hardware efforts have explored pinhole cameras, knife-edge collimators, and CC to improve detection efficiency and resolution. Software efforts focus on MC simulations and image reconstruction algorithms such as filtered back projection and Kernel Weighted Back Projection (KWBP) [16]. Despite these advancements, additional limitations persist related to the beam angle and the camera's relative orientation that may introduce variations in the observed image distortion patterns. Single-camera systems also suffer from limited angular coverage, which restricts their ability to capture a complete picture of PG distribution. Nonetheless, several works have demonstrated improved detector designs, reconstruction strategies, and system optimization for PG-based range verification, while also emphasizing constraints related to detection efficiency, background contamination, limited event statistics, and the tradeoff between spatial resolution and robustness in clinical conditions [20], [21], [22]. In particular, analyses of Compton imaging performance bounds have shown that efficiency and geometry strongly influence achievable range accuracy, motivating practical system configurations and correction strategies that remain compatible with clinical workflows [22].

In the present work, to address the limitations discussed above, we propose a novel configuration involving four CCs mounted on the gantry snout, forming a rectangular detection frame aligned with the beam axis. This fixed, compact geometry simplifies detector integration and avoids orientation shifts. We evaluated this quad-camera configuration using our Geant4-based Monte Carlo simulation platform, PJ-MC, which models patient anatomy and the full detection physics of the CCs. To assess and correct image distortion, we performed simulations with a virtual monoenergetic point source emitting 3 MeV photons at various positions inside the phantom. This source is not intended to represent a physical radioactive isotope, but rather an artificial emitter designed to approximate typical PG energies observed in proton therapy. Based on these, we developed a post-processing method called Point Source Normalization, which uses precomputed detector responses via PGE detected curve to iteratively correct spatial distortions in KWBP-reconstructed PG images. By integrating PSN into our workflow, we improved the spatial accuracy of PG hotspots, which is critical for reliable proton range verification. To our knowledge, this is the first study evaluating a quad-camera, snout-mounted PGI system. This paper is organized as follows: Section 2 describes the materials and methods used in the simulation and system modeling. Section 3 presents the results of the imaging performance and distortion analysis. Section 4 discusses the findings, and Section 5 concludes with a summary and future perspectives.

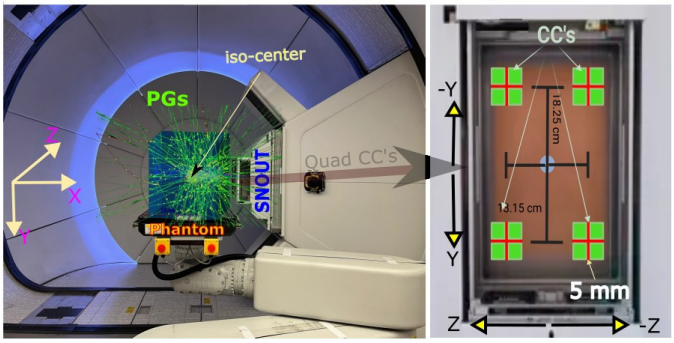

Fig. 1. (Color online) An illustration of an experimental setup for prompt-gamma imaging. (Left) Schematic view showing the proton beam, phantom, and simulated prompt-gamma (PG) trajectories. The isocenter and coordinate axes are indicated. (Right) A typical sketch of the quad-camera (QC) system mounted on the gantry snout. Each CC module consists of a 2×2 array of identical CZT crystals, separated by 5 mm, highlighted with a red solid line.

II. Materials and Methods

This study used our in-house Monte Carlo simulation code PJ-MC [17], based on GEANT4 [23], [24], [25], to model PG emission and detection during proton irradiation using CC detectors. The nuclear interaction models in PJ-MC were previously validated [26], and details of beam parameters and particle tracking can be found in our earlier work [27], [28], [29], [30]. This section provides a brief overview of the geometrical setup and simulation workflow in both water and patient-specific phantoms. The main focus is on PG behavior with a snout-mounted CC configuration and evaluation of ranges.

A. Quad-Camera Setup

An illustration of the experimental design under the proton gantry (proBeam Varian Medical Systems, Palo Alto, USA) is shown in Figure 1. The setup consists of four identical CC modules. Unlike traditional CC designs that use separate scatterer and absorber layers, the M3D gamma system employs monolithic pixelated Cadmium Zinc Telluride (CZT) crystals ($20 \times 10 \times 20$ mm with a 5 mm gap between crystals). Each module consists of a 2×2 array of identical crystals, with each crystal capable of recording multiple interactions, i.e. acting as both scatterer and absorber. The detector records individual gamma interactions by measuring their energy deposition, three-dimensional position (x, y, z), and timestamp. This data is then processed using reconstruction algorithm KWBP that identify Compton scattering sequences and estimate the direction or origin of the incident gamma rays. These camera modules are mounted symmetrically on a range shifter that is fixed to the gantry snout, forming a rectangular imaging geometry centered around the proton beam axis, as shown

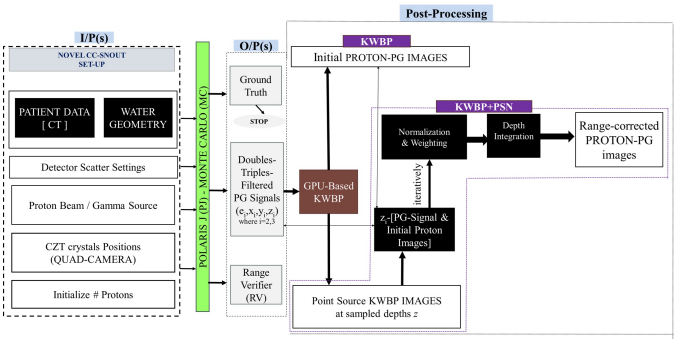

Fig. 2. (Color online) Workflow diagram illustrating the simulation and analysis pipeline used in this study. The process begins with setting up input parameters within the PJ-MC Monte Carlo framework. Prompt gamma events are filtered, stacked and send to GPU-based KWBP algorithm for reconstruction of the gamma images. A custom virtual point-source-based correction method (PSN) is applied at each samples depths 'z' to improve spatial accuracy using PG detected curve. This correction is called as KWBP+PSN and is used for proton range verification and image evaluation.

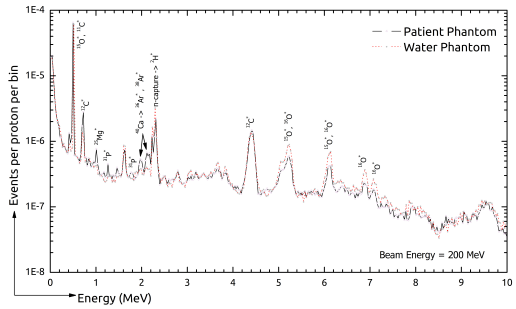

Fig. 3. (Color online) A typical prompt gamma ray spectrum detected in the CC for proton energies 200 MeV is presented. Most of the PG lines arose due to protons (secondary neutrons) reaction with abundant elements hydrogen, oxygen and carbon.

in Figure 1. The distance from the phantom's central axis (X = 0, Y = 0, Z = 0) to each detector module was 420 mm along the beam axis. In the present work, no shielding or collimators were included in the simulation to isolate the effects of the camera layout and geometry on prompt gamma detection and image formation. It may be mentioned that the intrinsic charge transport properties of CZT crystals were not explicitly modeled, detector timing behavior was approximated based on low-dose-rate performance metrics reported in our prior experimental studies [18], [31]. This allowed us to focus on spatial imaging trends rather than absolute count rates. The simulation study was structured in five stages i.e. (a) two scenarios using a homogeneous water phantom, (b) two with a CT-based prostate phantom, and (c) one scenario with mechanical displacement of the patient phantom and beam to simulate setup uncertainty. Proton beam energies of 70 MeV, 150 MeV, and 200 MeV were simulated to represent a range of clinically relevant treatment conditions. Beam parameters were based on clinical commissioning data [32].

B. Simulation Workflow Overview

The simulation workflow (Figure 2) begins with defining input parameters within the PJ-MC Monte Carlo framework. Patient CT data or water phantom geometries are selected based on the study type, and irradiation conditions are specified using either a clinical proton beam or a monoenergetic gamma source. At instance, in the case of patient-specific modeling, we used 3D CT volume of a prostate cancer patient, with in-plane resolution of 512 x 512 pixels with a slice thickness of 3 mm. HU values were converted to voxelized density/material maps using a pre-calibrated conversion curve [33]. The CC modules were localized to match the quad-camera, snout-mounted configuration described in Section II.A. During the Monte Carlo stage, PG events generated from proton-tissue nuclear interactions are tracked through the defined geometry and recorded by the detector modules. A typical prompt gamma ray spectrum detected in the CC from water and patient phantom for proton energies 200 MeV is presented in figure 3. As can be seen, a 0.511 MeV peak arises from positron annihilation following the decay of isotopes such as ^{15}O and ^{11}C. Dominant peak at 0.718 MeV PG line arises from the decay of ^{12}C*. The 2.22 MeV peak results from thermal neutron capture on hydrogen. At higher energies the 4.44 MeV line is produced by the de-excitation of ^{12}C*, while the 5.21 and 6.13 MeV lines correspond to de-excitations from ^{15}O* and ^{16}O*, respectively. Additional peaks in the patient phantom spectrum arise from proton-induced reactions on magnesium and phosphorus. Prompt gamma lines near 974 keV are attributed to the de-excitation of excited ^{25}Mg* nuclei, while the lines at approximately 1.266 MeV and 1.779 MeV correspond to transitions from excited ^{31}P* nuclei [34], [35], [36]. In addition, prompt gamma peaks observed at 1.97 MeV and 2.17 MeV in the present work can potentially be associated with transitions in ^{40}Ca, populated through reactions involving ^{38}Ar* and ^{36}Ar* [37]. Further, Compton scattering events, including single (where a PG undergoes no successive interactions and is absorbed in CC), double (where a PG undergoes two successive Compton interactions followed by full absorption), and triple scatters (three successive interactions), were recorded in the PGI system and are stacked in a list-mode dataset containing spatial and energy information for each interaction. These filtered PG signals are reconstructed using a GPU-accelerated kernel-weighted backprojection (KWBP) algorithm to produce initial PG images. A custom point-source normalization (PSN) method is then applied iteratively at sampled depths z to correct spatial variations using PGE and improve image fidelity. The resulting KWBP+PSN images are used for proton range verification and image evaluation. Furthermore, a range verification (RV) module of PJMC is activated using primitive scorers of Geant4 classes to record the proton depth dose profile in the phantom(s). The module is used to assess maximum depth dose (D_{max}) agreement with the RayStation-V11B treatment planning system [38] and are presented later in tables 2 and 3.

C. Description of Performed Simulations

To evaluate the proposed PGI system under different experimental and clinical conditions, three complementary simulation studies were performed:

1) Characterization of Gamma Detection Using a Monoenergetic Source: A virtual monoenergetic point source emitting 3 MeV photons was used to characterize the spatial response and image reconstruction behavior of the Compton camera. This study allowed quantitative assessment of geometric accuracy, attenuation effects, and the impact of the KWBP and PSN correction algorithms.
2) Snout-Mounted PGI Verification in Water and Patient Phantoms: The second study investigated the detection performance of the snout-mounted PGI system for both homogeneous (water) and heterogeneous (patient CT-based) phantoms. Point sources were placed at multiple depths along the beam axis to evaluate attenuation, geometry, and reconstruction accuracy under realistic anatomical conditions.
3) Sensitivity of the Snout-Mounted PGI to Range Deviations: The third study examined the system's sensitivity to proton range deviations caused by clinical setup uncertainties. Three conditions were simulated: a +10 mm anterior shift (Y-axis) of the proton beam (Condition 1), a reference case without a shift (Condition 2), and a -10 mm posterior shift (Y-axis) of the patient anatomy (Condition 3)

D. Image Reconstruction with KWBP

PG hotspots were reconstructed with a GPU-based KWBP algorithm [16], chosen for its efficiency and robustness to low-count data [17]. Only double and triple scatter events were used; single and $\geq$4-fold scatters were excluded to avoid ambiguity. Although single-scatter events are not used for image reconstruction, they are intentionally recorded to study detector-related effects, such as false coincidences, especially at higher event rates. For instance, two single events occurring simultaneously may mimic a double-scatter event, leading to false image artifacts. Having access to the full event set, including singles, allows us to apply our Monte Carlo Detector Effects (MCDE) framework [31] to model these scenarios and evaluate the system's performance under different dose-rate conditions. This is particularly valuable for extending this work toward future high-dose-rate applications. Further to maintain consistency and ensure fair comparison across different simulation scenarios, all reconstruction parameters were kept fixed throughout the study. The KWBP algorithm used a Gaussian kernel bandwidth of 15 voxels units, ran for 10 million iterations, and reconstructed onto a 3D grid of 200 $\times$ 200 $\times$ 200 voxels. The cone offset parameter was set to 0, maintaining alignment with the central axis during back-projection. This parameter defines the lateral displacement between the reconstructed Compton cone axis and the system's rotation (or imaging) axis. A value of zero therefore represents a perfectly centered projection cone, corresponding to the ideal back-projection geometry used in this study. This reconstruction framework enabled the generation of consistent PG images across both water and patient-specific phantoms under various beam energies, supporting the analysis of spatial distortions.

E. Point Source Simulation and Correction

To improve image accuracy and analyze distortion effects, we simulated virtual monoenergetic gamma point sources at different positions in both water and patient phantoms. Based on these simulations, we developed a post-processing correction method called the PSN method. This method uses precomputed detector responses from simulated point sources to iteratively correct spatial distortions in the KWBP-reconstructed PG images. The PSN method improves localization accuracy of PG hotspots, especially under conditions of limited detector coverage or signal sparsity. To improve the spatial accuracy of PG hot spots obtained via the KWBP algorithm, we implemented a correction method using precomputed responses from virtual monoenergetic gamma point sources at different depths. This approach uses a normalized system responses to adjust PG image intensity distributions at each depth increment. Let $\mathrm{M}^{(Z)}$ be the reconstructed PG image matrix at a given axial depth z for a monoenergetic point source, where $\mathrm{M}^{(Z)} \in \mathrm{R}^{n\times n}$ denotes a real-valued n$\times$n matrix and n = 200 (corresponding to the spatial grid resolution). For each Z, we define:

$$S^{(z)} = \sum_{i=1}^{n}\sum_{j=1}^{n} M_{ij}^{(z)} \tag{1}$$

This scalar $\mathrm{S}^{(z)}$ represents the total intensity of the reconstructed gamma distribution at depth z. The matrix is then rescaled to enhance the contrast of the hotspot:

$$\tilde{\mathbf{M}}^{(z)} = S^{(z)} \cdot \mathbf{M}^{(z)} \tag{2}$$

Afterwards, the rescaled matrix is weighted by the number of detected prompt gammas D(z) at that depth (extracted from the linear PG profile):

$$\mathbf{M}_{\mathrm{corr}}^{(z)} = D^{(z)} \cdot \tilde{\mathbf{M}}^{(z)} = D^{(z)} S^{(z)} \cdot \mathbf{M}^{(z)} \tag{3}$$

The final corrected PG image is then constructed iteratively by summing over all depths for which point source responses were computed:

$$\mathbf{M}_{\mathrm{final}} = \sum_{z\in\mathcal{Z}} \mathbf{M}_{\mathrm{corr}}^{(z)} \tag{4}$$

where $\mathcal{Z}$ is the set of discrete depths (e.g., $\mathcal{Z}$ = -150,-125,...,...,150 mm for the water phantom). The spacing of z values corresponds to the step size used in point-source simulation. It may be mentioned that the step sizes opted for the water and patient phantoms were not identical. For the homogeneous water phantom, a smaller step size (25 mm) was used to obtain a finer spatial sampling of the detected count distribution. For the patient phantom, derived from CT images, a coarser step size (50 mm) was chosen to cover the larger anatomical extent ($\pm$250 mm) while keeping the computational load reasonable. Since the purpose of this analysis

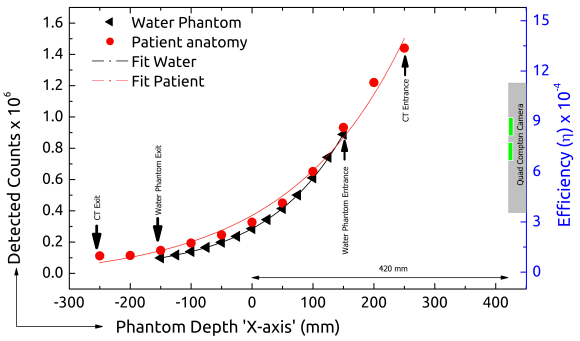

Fig. 4. (Color online) Detected count rates as a function of source–detector distance for the water and patient phantoms. The Quad CC system is positioned on the right side of the isocenter ($X = 0$ mm) at a distance of 420 mm. The water phantom was sampled in 25 mm steps from +150 mm to –150 mm, while the patient phantom (derived from CT data) was sampled in 50 mm steps from +250 mm to –250 mm. Slightly higher detected counts in the patient phantom arise from reduced effective attenuation caused by the presence of air and other low-density regions in the CT-based volume. The right-hand y-axis shows the corresponding detection efficiency (η) of the Quad CC. Camera geometry not to scale.

was to study the overall trend of the detected counts rather than a direct point-by-point comparison, the difference in step size does not affect the physical interpretation. Nevertheless, PSN process reconstructs a depth integrated, intensity weighted image that aligns more closely with the actual proton range, correcting for attenuation and angular bias present in the raw KWBP reconstructions.

1) Evaluation Metrics : PG images were evaluated qualitatively and quantitatively using:

1) PG Emission Range Deviation (Δ_{PGE}): The difference between the ground truth prompt gamma emission range and the proton range (D_{max}) estimated by RayStation and the in-house PJ-MC range verifier.
2) KWBP-Based PG Range Deviation (Δ_{KWBP}): The difference between the KWBP reconstructed PG range and the corresponding proton range.
3) KWBP+PSN PG Range Deviation ($\Delta_{KWBP+PSN}$): The difference between the reconstructed PG range after applying the PSN method and proton range D_{max}.

All range deviations were measured from beam entrance to the 100% and 90% falloff points in intensity and summarized in Tables 1 and 2.

III. Results

This section presents the characterization of PG emission and PGI performance under different conditions. First, gamma signals from the virtual monoenergetic sources were analyzed in both water and patient phantoms. Then, PG imaging for clinically relevant proton energies was evaluated using the snout-mounted Compton camera system. The impact of PSN correction was assessed across conditions. Both qualitative and quantitative outcomes are provided through figures and tables to support the observations.

1) Characterization of Gamma Detection Using a Monoenergetic Source: In clinical proton therapy, the PG energy spectrum typically spans from 0 to 9 MeV, comprising a range of emission lines from various nuclear reactions. This spectrum can be broadly described as having a three-fold distribution structure, with significant contributions appearing in the low (<3 MeV), mid (<3 to 6 MeVs), and high (>6 MeV) energy regions. To simplify the analysis and isolate geometric and detector-based effects, a virtual monoenergetic gamma source was defined at 3 MeV, which is selected as a representative midpoint or "folding point" of the overall PG spectrum. This choice allows to study the core spatial behavior of PG signal attenuation and its reconstruction, while reducing complexity introduced by multi-line spectral contributions.

The source was placed at multiple axial depths along the beam direction (X-axis), with a fixed lateral position (Y = 0, Z = 0). The PGI system remained at a fixed 420 mm distance from the isocenter in all cases, centered around the beam axis. At each depth, a total of 1.08×10^9 gamma events were simulated. Figure 4 shows the number of detected gamma events as a function of source depth in both phantoms. As expected, the number of detected events decreases as the source moves further from the camera system. This trend is attributed to a combination of the inverse square law and gamma attenuation, both of which reduce the likelihood of gammas reaching the detector from deeper positions. Notably, detection counts in the patient phantom were slightly higher than in the water phantom, especially at larger depths. For example, at +150 mm depth in the patient anatomy, the PGI system recorded $\approx 9.32\times10^5$ gamma events, compared to 8.89×10^5 events at +150 mm in the water phantom. At depth (-150 mm), detection counts fell to 1.46×10^5 in the patient case and 9.88×10^4 in the water case. This corresponds to a relative falloff of $\approx 84\%$ in patient anatomy and 89% in case of water phantom. The higher absolute counts observed in the patient phantom may result from anatomical differences in tissue composition that reduce the total attenuation along the detection path. The patient phantom, derived from CT data, includes soft tissue, bone, air, and external components such as the patient couch and clothing. As a result, the overall CT-bounding volume contains large regions of low-density material, leading to lower effective attenuation compared with the homogeneous water phantom.

To better describe the relationship between detected counts and source depth, an exponential model of the form $N(z)=a.e^{bz}+c$ was fitted to the data in both phantoms, where 'z' is the number of steps. As shown in Figure 4, the model captures the expected trend of exponential signal falloff with increasing depth. The fitted parameters indicate that the water phantom had a slightly steeper falloff rate (b = 0.0078 $\pm$ 0.0002) compared to the patient phantom (b = 0.0053 $\pm$ 0.0003). The uncertainties shown for the falloff rates represent standard deviation errors obtained from the fitted curve. This suggests that attenuation effects were slightly less pronounced in the patient phantom, consistent with the observed higher counts at large depths. Furthermore, the exponential model showed excellent agreement with the observed data, yielding R^2 = 0.9999 for the water phantom and R^2 = 0.9907 for the

TABLE I
DETECTED PG EVENTS USED FOR IMAGE RECONSTRUCTION AND CORRESPONDING DETECTION EFFICIENCY (η) OF THE QUAD COMPTON CAMERA (CC) FOR THE PATIENT PHANTOM (PP) AND WATER PHANTOM (WP). THE NUMBER OF GENERATED (EMITTED) PG EVENTS AT EACH PROTON ENERGY IS ALSO REPORTED.

Scatter Type	PP	η^{PP}	WP	η^{WP}
Energy = 200 MeV				
PG Emitted^{G}	212244600	–	403575300	–
Total PGs^{D}	239137	1.1E–3	146825	3.6E–4
Double PGs^{D}	17595	8.3E–5	11157	2.7E–5
Triple PGs^{D}	9208	4.3E–5	5948	1.5E–5
Energy = 150 MeV				
PG Emitted^{G}	143074800	–	164609460	–
Total PGs^{D}	214376	1.4E–3	138305	8.4E–4
Double PGs^{D}	15109	1.1E–4	9962	6.1E–5
Triple PGs^{D}	7710	5.4E–5	5206	3.2E–5
Energy = 70 MeV				
PG Emitted^{D}	44461500	–	52384080	–
Total PGs^{D}	108644	2.4E–3	72741	1.3E–3
Double PGs^{D}	6835	1.5E–4	4906	9.4E–5
Triple PGs^{D}	3420	7.6E–5	2402	4.6E–5

(G)→Generated PG events; (D)→Detected PG events.

patient phantom. Two-dimensional gamma image reconstructions across all source positions are illustrated in Figure 5(a,b). Panel (a) shows results in the water phantom, while panel (b) presents the same across the patient CT dataset. In both cases, the gamma hotspot is sharp and well-localized near the camera, and becomes more diffuse and less intense as depth increases. Despite these variations, the spatial trend remains clearly identifiable across all depths and phantom types.

2) Snout-mounted PGI verification: To evaluate PG hot spots under realistic treatment conditions, multiple simulations were performed at three clinically relevant proton beam energies: 70 MeV, 150 MeV, and 200 MeV, with beams along the Z-axis at the center of the phantom (X = 0, Y = 0). Each run used 1.08 $\times 10^9$ protons. PGs were recorded by the PGI system comprised of four CCs, which captured valid events through both direct interactions and secondary scattering processes. Table 1 summarizes, as an example, the qualitative data of PG events detected for each energy and phantom type.

Figure 6 illustrates the PG image reconstruction results in the water phantom. The top panel represents normalized linear profiles from its maximum value along the beam axis, including detected PG counts (dashed blue), reconstructed KWBP signal (green dash-dot), and the PG ground truth (solid red). The third row in the figure represents the 2D mapping of detected PG events. It can be seen that the detector PG strength gets weaker and weaker as protons traverse deeper into the phantom. This suggests that at higher energies a complete loss of PG events can be achieved at the proton maximum range (D_{max}-vertical red dashed line). Row 4 in the same figure represents the PG hot spots from the data shown in row 3 (PG detected) using the KWBP algorithm. It can be seen that for the lowest energy the PG hot spot reaches to D_{max}, however, at higher energies the physics of attenuation and inverse square law overwhelm the quality of PG events and thus affect the PG hot spots. This shows clearly that the higher the energy is the higher is the range discrepancy, i.e. an uncertainity Δ_{KWBP} of $\approx$ 70 mm is measured at 150 MeV proton energy which substantially increases to $\approx$ 176 mm at 200 MeV as presented in Table 2. A corrected profile, derived using a PSN method, is presented in row 5, revealing an improved alignment with the reference Δ_{PGE} as presented in row 2 termed as PGE. A similar behavior is observed in the patient anatomy as shown in Figure 7, and their qualitative values are tabulated in Table 2. Analysis shows that in both phantoms $\Delta_{KWBP+PSN}$ improved the agreement across energies. For instance, at 150 MeV, Δ_{KWBP} dropped from 53.09 mm to 42.67 mm (patient) and from 69.82 mm to 33.25 mm (water). PSN reduced range errors by $\sim$50-70$\%$ overall.

3) Sensitivity of the Snout-Mounted PGI in detecting range deviations due to patient or beam Shifts: To assess the proposed snout-mounted PGI system under clinical uncertainties, a reliability test was conducted by simulating isocenter shifts in a patient-specific phantom. Condition 1 (a, a1) simulates a +10 mm anterior shift of the proton beam along the Y-axis, mimicking a beam misalignment and Condition 3 (c, c1) applies a -10 mm posterior shift to the patient anatomy, while the beam remains fixed.

As shown in Figure 8, reconstructed PG distributions are presented for three shift conditions using both KWBP (top row, labeled a-c) and KWBP+PSN (row 2, labeled a1-c1) methods. The central column (b, b1) represents the reference case with no shift. While similar to the 200 MeV results shown in Figure 6, where PSN correction was based on patient data, this section uses water phantom data for PSN calculation. This allows us to test whether water-derived corrections can be reliably applied to patient anatomy. The isocenter was placed at coordinates (0, 0, -65.91 mm) from the PGI system, with the system mounted 420 mm from the patient central axis on the gantry snout. This setup corresponds to a proton beam of 200 MeV, with a calculated D_{max} of 251.04 mm, marked by the vertical dashed line in Fig. 7(b,b1) without a shift. It may be mentioned that each shift in beam or anatomy caused a shift in the actual D_{max} by approximately 3.47 mm. The corrected images captured this shift effectively, which is illustrated in row 3 of Figure 8(d-f), underscoring the spatial accuracy of the correction algorithm. In Figure 8(g-h), i.e. row 4, the profiles along the Y-axis are illustrated to evaluate whether the system can detect shifts in the anterior-posterior (Y-axis) direction. The results are encouraging that both KWBP and PSN methods are able to identify beam and patient shifts, although the PSN method provides slightly more consistent and accurate localization.

These observations are quantitatively summarized in Table 3. It may be mentioned that the statistical uncertainty was tested by repeating simulations with reduced proton counts (10^2 times), which resulted in an average deviation of about $\pm$ 14$\%$ in Δ_{KWBP} and $\Delta_{KWBP+PSN}$ while Δ_{PGE} showed only $\pm 2\%$.

IV. DISCUSSIONS

This study introduces a novel configuration for PGI, where a CC system is mounted directly on the snout of a clinical

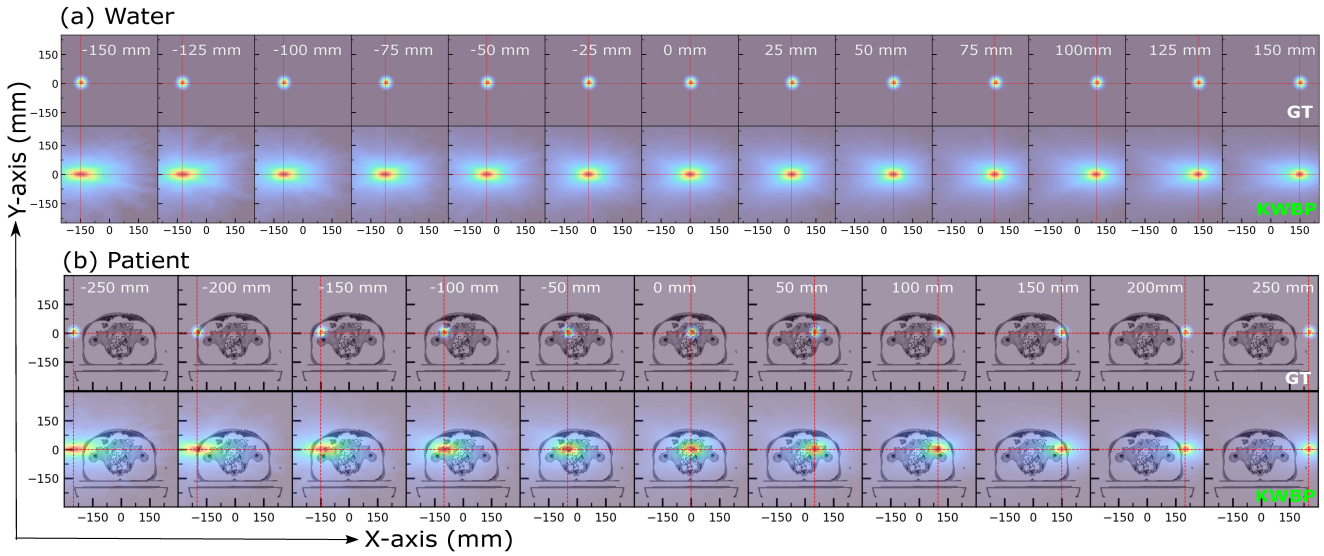

Fig. 5. (Color Online) Reconstructed 2D PG distributions for a 3 MeV virtual monoenergetic source placed at different depths along the beam axis (X-axis). (a) Water phantom in 25 mm steps (-150 to +150 mm). (b) Patient anatomy in 50 mm steps (-250 to +250 mm). The coordinate system is defined such that +Y corresponds to posterior, -Y to anterior, -X represents increasing depth along the beam axis (toward the distal side), and +X points toward the beam entrance. GT denotes the ground-truth distribution from PJ-MC, and KWBP is the reconstructed image using the KWBP method. Red dashed lines indicate the central Y-X coordinates of the source position; their intersection marks the nominal source location at each depth step. In both cases, the signal intensity decreases with depth due to attenuation. In the patient phantom, additional distortion and stretching of the PG spot are visible at deeper (-X) positions, particularly beyond -150 mm, reflecting the effects of anatomical heterogeneity and the increased attenuation associated with longer source to detector distance resulting longer paths for gammas.

TABLE II
COMPARISON OF PROMPT GAMMA EMISSION, KWBP AND POINT SOURCE NORMALIZED KWBP+PSN DEVIATION ACROSS DIFFERENT ENERGIES FOR WATER AND PATIENT PHANTOMS.

Proton Energy (MeV)	Proton Range/D_{max} PJ–MC (mm)	Proton Range RayStat.-V11B (mm)	$^1\Delta_{KWBP}$ (mm)	$^1\Delta_{KWBP+PSN}$ (mm)	$^1\Delta_{PGE}$ (mm)
Water Phantom					
At 100% of peak value at $D_{\max}$					
200	252.7	253.50	176.40	56.58	18.71
150	152.04	153.50	69.82	33.25	16.07
70	38.79	39.50	17.25	17.10	16.25
At 90% of peak value at $D_{\max}$					
200	252.7	253.50	133.40	14.52	14.52
150	152.04	153.50	25.30	6.06	12.70
70	38.79	39.50	30.07	42.09	14.33
Patient Phantom					
At 100% of peak value at $D_{\max}$					
200	251.04	250.10	143.97	47.90	9.04
150	153.27	154.20	53.09	42.67	13.27
70	42.57	41.30	16.47	8.17	8.17
At 90% of peak value at $D_{\max}$					
200	251.04	250.10	72.80	1.10	2.45
150	153.27	154.20	7.49	3.04	12.67
70	42.57	41.30	6.42	12.68	8.17

^{1}Note $\rightarrow$ Deviation calculations were made using $D_{\max}$.

proton gantry (ProBeam), as illustrated in Figure 1. A full Monte Carlo simulation workflow was employed using a custom-developed platform, PJMC [16], to simulate proton-induced prompt gamma emissions and their interactions in both a homogeneous water phantom and a patient-specific prostate anatomy. Image reconstruction was performed using the KWBP algorithm as a post-processing step to localize prompt gamma hotspots. All data were collected by the PGI system positioned 420 mm from the isocenter and oriented at 90^0 relative to the proton beam axis. The overall simulation and analysis workflow, from phantom selection to PG image reconstruction, is illustrated in Figure 2. The resulting

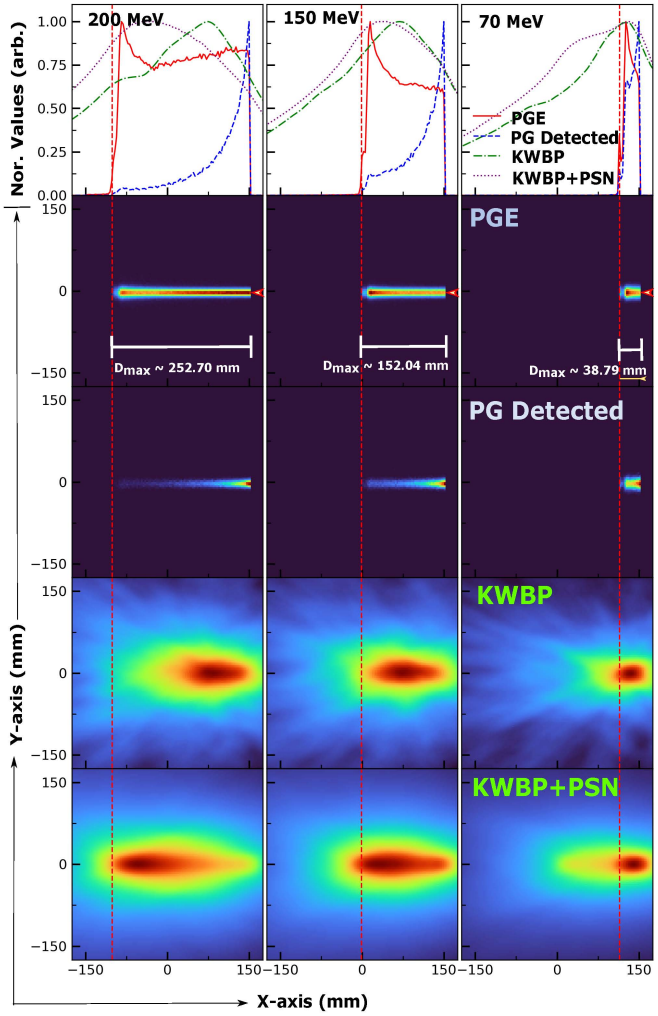

Fig. 6. (Color online) PG imaging and reconstruction results in the water phantom for three proton beam energies (200, 150, and 70 MeV). Top row: Normalized 1D profiles along the beam axis (X-axis) showing prompt gamma emission (PGE, red), detected PGs (blue dashed), reconstructed images using KWBP (green dashed-dotted), and PSN-corrected KWBP (black dotted). Subsequent rows: 2D spatial distributions corresponding to each case, arranged from top to bottom as PGE, PG detected, KWBP, and KWBP+PSN. The vertical red dashed line indicates the position of the distal dose maximum (D_{max}), while the beam entrance direction is marked by the red arrowhead in row 2. The coordinate system is defined such that +Y corresponds to posterior, -Y to anterior, -X represents increasing depth along the beam axis (toward the distal side), and +X points toward the beam entrance.

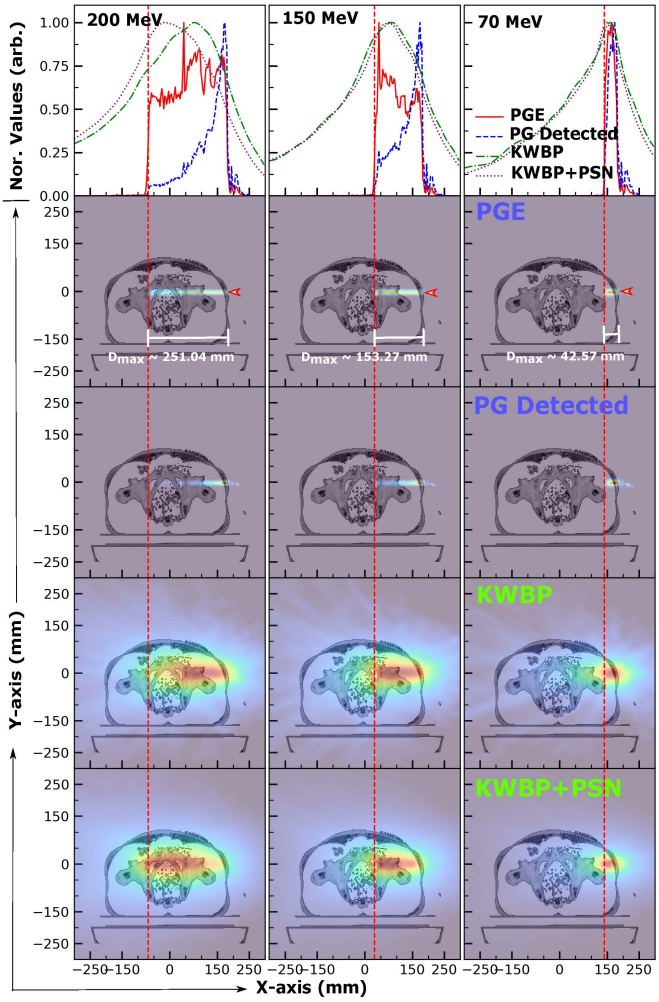

Fig. 7. (Color online) PG imaging and reconstruction results in the patient phantom for three proton beam energies (200, 150, and 70 MeV). Top row: Normalized 1D profiles along the beam axis (X-axis) showing prompt gamma emission (PGE, red), detected PGs (blue dashed), reconstructed images using KWBP (green dashed-dotted), and PSN-corrected KWBP (black dotted). Subsequent rows: 2D spatial distributions corresponding to each case, arranged from top to bottom as PGE, PG detected, KWBP, and KWBP+PSN. The vertical red dashed line indicates the position of the distal dose maximum (D_{max}), while the beam entrance direction is marked by the red arrowhead in row 2. The coordinate system is defined such that +Y corresponds to posterior, -Y to anterior, -X represents increasing depth along the beam axis (toward the distal side), and +X points toward the beam entrance.

gamma spectra is presented in Figure 3 and detected gamma trend is shown in Figure 4, reflects the expected decrease in detected PG events as the source moves deeper into the phantom, largely due to geometric dispersion (inverse square law) and attenuation effects. An exponential fitting showed a steeper gamma counts falloff rate in the water phantom when compared to the patient phantom attributed to heterogeneous anatomy and the presence of low-density regions.

The two-dimensional PG reconstructions shown in Figure 5 provide further insight into how image quality degrades with source depth in both phantoms. As expected, hotspots closer to the PGI system appear well-localized and intense, while those at greater depths become progressively broader and attenuated. Nonetheless, the KWBP algorithm is effective at reconstructing the spatial origin of gamma emissions from the monoenergetic source, however, it does not take into account how proton beams actually lose energy and deposit dose (D_{max}). As a result, in deeper regions or in anatomically heterogeneous areas, KWBP alone is not sufficient to accurately identify the true range of the proton beam without applying an additional correction method, such as the PSN approach used in this study.

Simulations were performed at three clinical proton beam energies: 70 MeV, 150 MeV, and 200 MeV; as shown in Figures 6 and 7, along with the range error metrics in Table 2, the reconstruction results reveal strong energy-dependent limitations when relying on the KWBP algorithm. In particular,

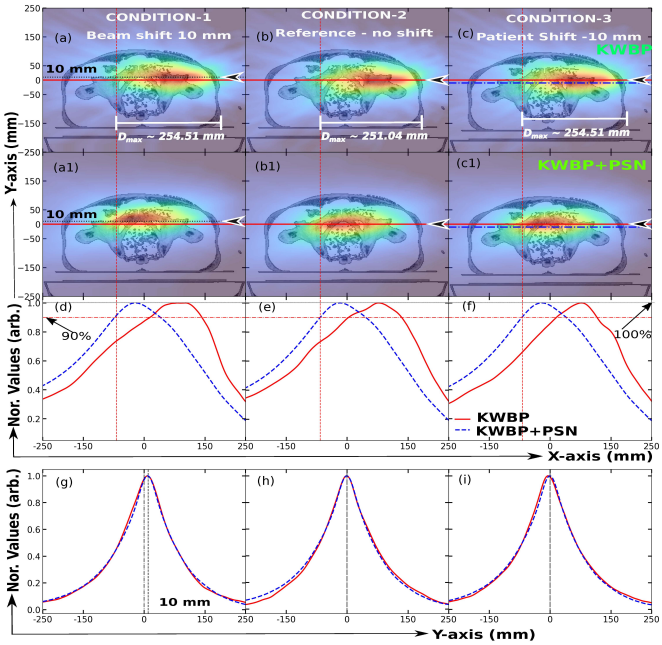

Fig. 8. (Color online) Combined results for proton range verification in the patient phantom under three shift conditions: Condition 1: Beam shifted posteriorly (+Y-axis) by 10 mm; Condition 2: Reference (no shift); Condition 3: Patient shifted anteriorly (-Y-axis) by -10 mm. Top two rows (a-c and a1-c1) show corresponding 2D PG hot spots for KWBP and KWBP+PSN image reconstruction methods. Bottom two rows (d-f and g-i) present linear profiles of the deduced data with respect to depth and anterior-posterior misalignments. D_{max} (or depth dose profile maximum) was measured from the entrance point of the patient body and is marked by the arrowhead in row 1 & 2 . The coordinate system is defined such that +Y corresponds to posterior, -Y to anterior, -X represents increasing depth along the beam axis (toward the distal side), and +X points toward the beam entrance.

TABLE III
COMPARISON OF PG RANGE DEVIATIONS UNDER ISOCENTER SHIFTS, EVALUATED AT 100% AND 90% OF $D_{\max}$. A 2.2% UNCERTAINTY HAS BEEN OBSERVED IN ALL MEASURED VALUES DURING THE SIMULATION RUNS.

Conditions	PJ-MC (mm)	RayStation-V (mm)	Δ_{KWBP} (mm)	$\Delta_{KWBP+PSN}$ (mm)
At 100% of Peak Value at $D_{\max}$				
Beam Shift	254.51	253.25	152.25	47.25
No Shifts	251.04	250.10	143.91	47.91
Patient Shift	254.51	253.25	146.19	47.19
At 90% of Peak Value at $D_{\max}$				
Beam Shift	254.51	253.25	82.85	3.97
No Shifts	251.04	250.10	69.69	0.14
Patient Shift	254.51	253.25	84.03	1.06

KWBP reconstructions consistently underestimated the Bragg peak (D_{max}), with discrepancies increasing significantly at higher proton energies. At the 100% dose level, the water phantom showed KWBP range errors growing from 17.25 mm at 70 MeV to 69.82 mm at 150 MeV, and further to 176.40 mm at 200 MeV. Similarly, in the patient phantom, the discrepancies were 16.47 mm, 53.09 mm, and 143.97 mm for 70, 150, and 200 MeV, respectively. A similar pattern is observed at the 90% D_{max} level; in some cases, the PG signal extends beyond D_{max}, due to the broader nature of the PGE profile at lower detection thresholds. To mitigate these effects, a post-processing correction strategy using the PSN method was implemented. By convolving pre-characterized 2D response matrices from monoenergetic 3 MeV sources at various depths, this method adjusts the spatial profile of the KWBP output to better match the true gamma emission distribution. The result is a significantly improved alignment between the reconstructed PG range and the known D_{max}. In the patient phantom case, the corrected results showed substantial error reduction: at 70 MeV, the error decreased from 16.47 mm to 8.17 mm (50.4% improvement); at 150 MeV, from 53.09 mm to 42.67 mm (19.6% improvement); and most impressively, at 200 MeV, from 143.97 mm to 47.90 mm (63.7% improvement). In the water phantom, the improvements were even more pronounced: a marginal gain of 0.86% at 70 MeV (17.25 mm to 17.10 mm), 52.4% at 150 MeV (69.82 mm to 33.25 mm), and 67.9% at 200 MeV (176.40 mm to 56.58 mm).

Further validation of the entire PGI workflow, including prompt gamma generation using the PJMC simulation, image reconstruction with the KWBP algorithm, and correction using the PSN method, was carried out using three Y-axis shift scenarios in a patient-specific phantom and are presented in figure 8. These simulations were performed at a proton beam energy of 200 MeV, which was intentionally chosen because it showed the largest range discrepancy (Δ_{KWBP}) and the highest attenuation effects compared to lower energies. The shift conditions representing realistic setup uncertainties that could occur during treatment, however, once the PSN method was applied the PG distributions shifted significantly closer to the true dose endpoints. For example, in Condition 1:Beam shift (+10 mm) at the clinically important 90% D_{max} level, the PG range deviation improved from 82.85 mm (KWBP) to 3.97 mm (KWBP+PSN). Similar improvements were observed for the condition 2: reference (69.69 $\longrightarrow$ 0.14) and for condition 3:patient shift (84.03 $\longrightarrow$ 1.06 mm) setups.

V. CONCLUSIONS

We proposed and evaluated a novel snout-mounted PGI system using a quad CC configuration for in vivo proton range verification. Comprehensive MC simulations using the PJ-MC platform demonstrated the feasibility of this geometry in both water and patient-specific phantoms. While KWBP-based reconstructions showed increasing range deviations with higher proton energies due to attenuation and geometric losses, the implementation of a PSN method under PGE detected responses significantly reduced these discrepancies. Range errors were reduced by up to 70% in both phantom types. Addi-tionally, the PSN method showed robustness in detecting millimeter-scale range shifts under simulated beam and patient misalignments, even when correction parameters were derived from idealized water data. These findings suggest that the snout-mounted PGI configuration, combined with PSN, can provide accurate and non-invasive proton range verification. Future work will focus on experimental validation of the system.

ACKNOWLEDGMENT

V R S, J C P, L R acknowledge the support from National Institutes of Health under Grants No. R01-CA279013 and R01-EB032680. VRS wants to thank Dr. F Farokhi (Dept. of Medical Physics, INFN-LNS, Catania, Italy) for all her support during data structuring. Further, VRS thanks H. Lewis for computational support. All authors declare that they have no known conflicts of interest in terms of competing financial interests or personal relationships that could have an influence or are relevant to the work reported in this paper.

REFERENCES

[1] P. Everaere *et al.*, "Prompt-gamma energy integration: a new method for online-range verification in proton therapy with pulsed beams," *Frontiers in Physics*, vol. 12, p. 1371015, 2024.

[2] B. W. Cheon and C. H. Min, "Prompt gamma imaging system in particle therapy: a mini-review," *Frontiers in Physics*, vol. 12, p. 1356572, 2024.

[3] M. Kołodziej, "Construction and characterisation of a coded-mask gamma camera for beam range monitoring in proton therapy," *arXiv*, 2025.

[4] C. M. Scaffaro-Karlsen *et al.*, "Prompt gamma-ray imaging in realistic background conditions of a boron neutron capture therapy environment," *Scientific Reports*, vol. 15, p. 18626, 2025.

[5] G. Borghi *et al.*, "First experimental verification of prompt gamma imaging with carbon ion irradiation," *Scientific Reports*, vol. 14, p. 25750, 2024.

[6] E. Draeger *et al.*, "3d prompt-gamma imaging for proton beam range verification," *Physics in Medicine and Biology*, vol. 63, p. 035019, 2018.

[7] E. Muñoz *et al.*, "Proton range verification with MACACO II Compton camera enhanced by a neural network for event selection," *Scientific Reports*, vol. 11, p. 9325, 2021.

[8] S. Bertschi *et al.*, "Feasibility of prompt gamma verification for cone-beam CT-based online adaptive proton therapy," *Physics and Imaging in Radiation Oncology*, vol. 34, p. 100778, 2025.

[9] I. Meric *et al.*, "A hybrid multi-particle approach to range assessment-based treatment verification in particle therapy," *Scientific Reports*, vol. 13, p. 6709, 2023.

[10] M. Testa *et al.*, "Monitoring the Bragg peak location of 73 MeV protons by means of prompt gamma-ray measurements," *Applied Physics Letters*, vol. 93, p. 093506, 2008.

[11] C. H. Min *et al.*, "Prompt gamma measurements for locating the dose falloff region in proton therapy," *Applied Physics Letters*, vol. 89, p. 183517, 2006.

[12] C. Golnik *et al.*, "Range verification in proton therapy based on prompt gamma-ray timing measurements," *Physics in Medicine and Biology*, vol. 59, pp. 5399–5422, 2014.

[13] C. Richter *et al.*, "First clinical application of a prompt gamma-based in vivo proton range verification system," *Radiotherapy and Oncology*, vol. 118, no. 2, pp. 232–237, 2016.

[14] M. Pinto, "Prompt-gamma imaging in particle therapy," *European Physical Journal Plus*, vol. 139, p. 884, 2024.

[15] M. Pinto *et al.*, "Prompt gamma imaging with a Compton camera for in vivo range verification of proton therapy: a proof of principle," *Physics in Medicine and Biology*, vol. 59, pp. 7653–7669, 2014.

[16] R. Panthi *et al.*, "Secondary particle interactions in a Compton camera designed for in vivo range verification of proton therapy," *IEEE Transactions on Radiation and Plasma Medical Sciences*, vol. 5, pp. 383–391, 2021.

[17] V. R. Sharma *et al.*, "Modeling prompt gamma emission, detection and imaging in real patient anatomy using a novel Compton camera for dose verification in proton therapy," *Physics in Medicine and Biology*, vol. 70, no. 12, p. 125004, 2025.

[18] Z. Jiang *et al.*, "A feasibility study of enhanced prompt gamma imaging for range verification in proton therapy using deep learning," *Physics in Medicine and Biology*, vol. 68, p. 075001, 2023.

[19] J. Berthold *et al.*, "First-in-human validation of CT-based proton range prediction using prompt gamma imaging in prostate cancer treatments," *International Journal of Radiation Oncology Biology Physics*, vol. 111, no. 4, pp. 1033–1043, 2021.

[20] L. Rebolo *et al.*, "Cherenkov light emission in pure Cherenkov emitters for prompt gamma imaging," *IEEE Transactions on Radiation and Plasma Medical Sciences*, vol. 8, no. 1, 2024.

[21] H. Zhang *et al.*, "Proton range verification realized via a multislit prompt gamma imaging system," *IEEE Transactions on Radiation and Plasma Medical Sciences*, vol. 9, no. 8, 2025.

[22] D. Shy *et al.*, "Cramér–Rao bound evaluations of Compton imager designs for proton beam range verification," *IEEE Transactions on Radiation and Plasma Medical Sciences*, vol. 6, no. 6, 2022.

[23] S. Agostinelli *et al.*, "Geant4—a simulation toolkit," *Nuclear Instruments and Methods in Physics Research Section A*, vol. 506, pp. 250–303, 2003.

[24] J. Allison *et al.*, "Geant4 developments and applications," *IEEE Transactions on Nuclear Science*, vol. 53, pp. 270–278, 2006.

[25] ——, "Recent developments in Geant4," *Nuclear Instruments and Methods in Physics Research Section A*, vol. 835, pp. 186–225, 2016.

[26] J. Jeyasugiththan and S. W. Peterson, "Evaluation of proton inelastic reaction models in Geant4 for prompt gamma production during proton radiotherapy," *Physics in Medicine and Biology*, vol. 60, pp. 7617–7635, 2015.

[27] S. W. Peterson *et al.*, "Experimental validation of a Monte Carlo proton therapy nozzle model incorporating magnetically steered protons," *Physics in Medicine and Biology*, vol. 54, pp. 3217–3229, 2009.

[28] S. W. Peterson, D. Robertson, and J. Polf, "Optimizing a 3-stage Compton camera for measuring prompt gamma rays emitted during proton radiotherapy," *Physics in Medicine and Biology*, vol. 55, pp. 6841–6856, 2010.

[29] J. Polf *et al.*, "Prompt gamma-ray emission from biological tissues during proton irradiation: a preliminary study," *Physics in Medicine and Biology*, vol. 54, pp. 731–743, 2009.

[30] J. C. Polf *et al.*, "Measurement of characteristic prompt gamma rays emitted from oxygen and carbon in tissue-equivalent samples during proton beam irradiation," *Physics in Medicine and Biology*, vol. 58, pp. 5821–5831, 2013.

[31] P. Maggi *et al.*, "Computational model for detector timing effects in Compton-camera based prompt-gamma imaging for proton radiotherapy," *Physics in Medicine and Biology*, vol. 65, p. 125004, 2020.

[32] C. F. Groenendijk *et al.*, "A Geant4-based simulation platform of the HollandPTC R&D proton beamline for radiobiological studies," *Physics in Medicine and Biology*, vol. 68, no. 4, p. 045001, 2023.

[33] W. Schneider, T. Bortfeld, and W. Schlegel, "Correlation between CT numbers and tissue parameters needed for Monte Carlo simulations of clinical dose distributions," *Physics in Medicine and Biology*, vol. 45, pp. 459–478, 2000.

[34] M. Zarifi, S. Guatelli *et al.*, "Characterization of prompt gamma ray emission for in vivo range verification in particle therapy: a simulation study," *Physica Medica*, vol. 62, p. 20, 2019.

[35] M. Hyvonen-Dabek, "Proton-induced prompt gamma-ray emission for determination of light elements in human bone," *Journal of Radioanalytical Chemistry*, vol. 63, no. 2, pp. 367–378, 1981.

[36] W. Yahia-Cherif *et al.*, "Measurement and analysis of nuclear γ-ray production cross sections in proton interactions with Mg, Si, and Fe nuclei over the incident energy range $e = 30$–66 MeV," *Physical Review C*, vol. 102, p. 025802, 2020.

[37] D. Newton *et al.*, "Reactions induced in ^{40}Ca by 150 MeV protons," *Nuclear Physics*, vol. 82, pp. 499–512, 1966.

[38] M. Janson *et al.*, "Treatment planning of scanned proton beams in RayStation," *Medical Dosimetry*, vol. 49, pp. 2–12, 2024.